Design and Implementation of a Shape Memory Alloy Actuated Reconfigurable Airfoil

Justin K. Strelec[a], Dimitris C. Lagoudas[a]
[a]Aerospace Engineering Department, Texas A&M University, College Station, TX 77843-3141
Mohammad A. Khan[b], John Yen[b]
[b]Computer Science Department, Texas A&M University, College Station, TX 77843-3112

ABSTRACT

The unique thermal and mechanical properties exhibited by shape memory alloys (SMAs) present exciting design possibilities in the field of aerospace engineering. When properly trained, SMA wires act as linear actuators by contracting when heated and returning to their original shape when cooled. These SMA wire actuators can be attached to points on the inside of an airfoil, and can be activated to alter the shape of the airfoil. This shape-change can effectively increase the efficiency of a wing in flight at several different flow regimes. To determine the necessary placement of the SMA wire actuators within the wing, a global optimization method that incorporates a coupled structural, thermal, and aerodynamic analysis has been utilized. A genetic algorithm has been chosen as the optimization tool to efficiently converge to a design solution. The genetic algorithm used in this case is a hybrid version with global search and optimization capabilities augmented by the simplex method with selective line search as a local search technique. A cost function based on the aerodynamic properties of the airfoil has been used to optimize this design problem to maximize the lift-to-drag ratio for a reconfigured airfoil shape at subsonic flow conditions. A wind tunnel model reconfigurable wing was fabricated based on the design optimization to verify the predicted structural and aerodynamic response. Wind tunnel tests indicated an increase in lift for a given flow velocity and angle of attack by activating the SMA wire actuators. The pressure data taken during the wind tunnel tests followed the trends expected from the numerical pressure results.

Keywords: shape memory alloy, reconfigurable wing, SMA actuator, finite element method, computational fluid dynamics, genetic algorithm, simplex method, design optimization

1. INTRODUCTION

Aircraft design involving fixed wing structures often involves a sacrifice in design point efficiency to account for off-design flight conditions. These compromises can be eliminated with the implementation of a wing that can adapt to its current flow condition. Many modern aircraft already utilize this adaptable wing technology in some form. Variable sweep wings and variable pitch propellers both reconfigure a structural aspect of the wing to achieve a desired increase in efficiency. Leading and trailing edge high-lift devices, such as flaps, can be deflected to greatly increase a wing's lift for takeoff and landing.

1.1 Reconfigurable Airfoils

One factor that greatly influences a wing's efficiency at a particular flow regime is the shape of its cross-section, or airfoil. Some airfoils are aerodynamically efficient at subsonic speeds, but tend to create undesirable shock waves early in the transonic regime. Other airfoils are tailored to minimize wave drag near the speed of sound, but do not produce very favorable pressure distributions at low subsonic speeds. Typical plots of favorable pressure distributions in subsonic and transonic regimes are shown in Figure 1 [1]. Airfoils are usually designed with a primary flight condition in mind, for instance a cruise condition of 0.85 Mach. These airfoils are generally sub-optimal for the design point because they are fixed and must be used at takeoff, landing, climb, and descent, in addition to the design point condition. It would be desirable to have an airfoil with the ability to adapt to its current flow regime and alter its shape to remain efficient at any speed.

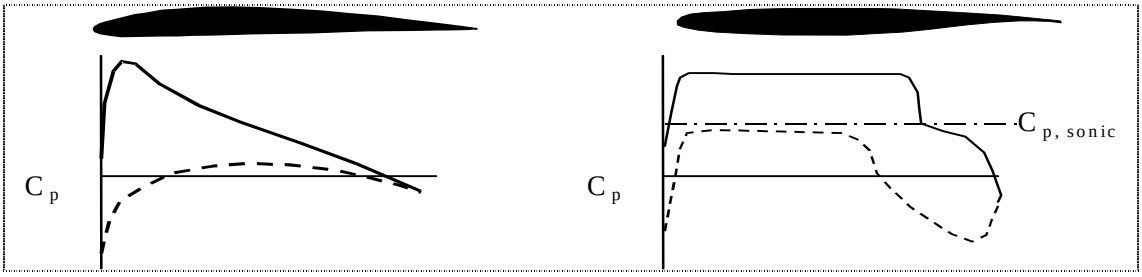

Figure 1. Pressure plots of typical subsonic (left) and transonic (right) airfoils in their respective flow regimes

The deformation of an airfoil's shape can be achieved in two ways – through aerodynamic and structural means. The first approach focuses on altering the "virtual shape" of the airfoil, or the shape that the flow actually "sees", without deforming the physical structure in any way. One type of aerodynamic shape control uses synthetic jets to energize the flow around an airfoil. This can be achieved by continuous or intermittent blowing and sucking to energize the flow near the surface of the airfoil, but is highly sensitive to flow velocity and is typically used to fine-tune the shape of the flow [2]. Other flow control methods that have been investigated energize the flow acoustically or mechanically [3,4].

The second approach, and the primary focus of this research, is based on altering the physical shape of the airfoil. This research focuses on developing a method to control the shape of an airfoil in a global sense. That is, to create a reconfigurable wing whose airfoil can achieve the potential large-scale deflections necessary to maintain high efficiency as flow conditions change. Reconfigurable airfoil technology can increase efficiency, maneuverability, and control, but must also meet weight, cost, and structural feasibility restraints (such as location of fuel, landing gear, etc. within the wing) to be considered practical. The application scope of the reconfigurable airfoil is very broad, including micro aerial vehicles, uninhabited vehicles, conventional full-scale aircraft, ornithopters (flapping flight), and submersibles [5,6].

Much of the recent work in the area of reconfigurable airfoil structures has focused on locally deforming a portion of an airfoil to achieve some specific single design point goal. Typical applications include the actuation of leading and trailing edge devices [7] as well as small-scale surface deflections to increase performance in a specific flow regime [8]. A major hindrance in the development of a reconfigurable airfoil has been the bulky nature of available actuators that can provide enough force to overcome the structural stiffness of the wing and achieve this shape change. Available space within the wing and the weight of the actuator are design restrictions that can be difficult to overcome with conventional actuators.

1.2 Active Materials as Actuators

Recently, much attention has been given to creating actuator systems out of active materials. Piezoelectric actuators have been examined for the shape control of beams [9] and as active shape control devices used to improve an aircraft's aeroelastic response [10]. When implemented as piezoelectric stacks, they have been used to deflect trailing edge flaps on helicopter rotor blades [11]. Some researchers have used them to control wake vortices, dampen wing flutter, and prevent flow separation over a wing [12,13]. Magnetostrictive actuators demonstrate high frequency, low stroke characteristics. These actuators have been investigated for use as active vibration control devices [14]. A high force, high displacement actuator is needed to achieve the deformations required for full airfoil reconfigurability. Current research of shape memory alloys has revealed that they can be used very effectively as lightweight, high force, large deflection, quick-response actuators that may be ideally suited for the reconfigurable airfoil application [15,16].

Shape memory alloy actuators are activated by a change in temperature and can take several forms. SMA torque tubes, strips, and wires are all potential candidates for the type of actuation needed for the

reconfigurable airfoil. SMA torque tubes have been used to generate variable twist in an adaptable wing, but cooling the torque tube was complicated and expensive [17,18]. SMA wires can be heated by electrical resistance and cooled by free convection. This simple actuation method has led many researchers to use them as linear actuators. Researchers have used SMA wires to actuate adaptive spoiler bumps to control transonic shock waves [19], and to deflect both conventional and hingeless control surfaces [20-25].

Shape memory alloys (SMA) are set apart from other metals by their unique crystalline characteristics [26]. They exhibit one of two crystalline lattice structures depending on the applied stress and temperature. The low temperature phase, martensite, consists of monoclinic variants and the high temperature phase, austenite, is a body centered cubic arrangement. The material properties of SMA are dependant on the amount of each phase present at a given time.

The martensitic phase of an SMA can have a lattice arrangement in one of 24 variants depending on the local stress field, and can appear as twinned or detwinned. In its martensitic phase, SMA can be deformed easily as these variants interchange to those that align more favorably with the local stress field. Heating the SMA will force a return to its austenitic phase and bring the SMA back to its original macroscopic shape. The recovered strain is called the transformation strain, corresponding to one-way shape memory effect. Two-way shape memory effect can be achieved by inducing a plastic deformation in the material such that a transformation into martensite results in a macroscopic shape change without an applied stress. This is called two-way shape memory effect because macroscopic shape change occurs in both the heating and cooling directions, even in the absence of external stresses [27].

Because they are both commonly attainable and relatively easy to implement as linear actuators, SMA wires will be used in this research. Two-way trained SMA wire actuators can be attached to points on the inside of an airfoil after they have been cooled below the martensitic finish temperature. When the wires are heated above the austenitic start temperature, they begin to contract, recovering the transformation strain and deforming the airfoil. Upon cooling below the martensitic finish temperature, the SMA actuators are brought back to their original configuration, returning the airfoil to its original shape.

To be fully effective, a reconfigurable airfoil should be capable of continuous shape change to achieve an optimal shape at multiple design points. Each design point may require a different airfoil shape, based on flight variables such as Mach number, Reynolds number, and angle of attack. This type of continuous morphing airfoil would require multiple actuators and/or precise temperature regulation for each desired airfoil shape. The number of SMA actuators, the transformation strain of the SMA, and the location of the actuators within the reconfigurable airfoil are major factors in determining how the airfoil will deform when the actuators are activated. However, with these variables and the continuous morphing airfoil concept in mind, the number of possible actuator combinations within the airfoil is nearly infinite. A global design optimization is required to circumvent a potentially large number of local minima and determine the true optimal actuator configuration.

1.3 Genetic Algorithm Design Optimization

Genetic algorithms (GAs) have proven to be effective for a wide variety of complex optimization problems. They are particularly useful in problems where the search space has numerous local optima, as traditional optimization methods can easily become trapped. For example, GAs have been used to find the coordinates of an airfoil from a given surface pressure distribution [28]. In another example, a GA combined with aerodynamic evaluation from XFOIL is used to find the rotor airfoil shape that maximizes lift-to-drag and minimizes noise [29]. GAs have also been demonstrated as modeling, design optimization, and control tools for piezoelectric actuators on plates for vibration control applications [30, 31, 32].

Genetic algorithms are used as global search and optimization techniques, and are based on the concept of evolution and natural selection [33]. These methods search for optima by maintaining a set of candidate

solutions and incrementally improving the solution using genetically inspired operators. Each solution is assigned a fitness value based on some function intended to capture the optimization goal.

The disadvantage of the genetic algorithm is its slow convergence rate. GAs focus on globally exploring the search space based on essentially random operators while local optimization techniques follow the most promising direction to find an optimal solution in short computational time with decreased reliability. A common strategy is to combine a GA with a local search technique to decrease convergence times while maintaining the global search benefits of the GA. One such local search technique is called the simplex method. A hybrid GA-simplex method is examined for use with the reconfigurable airfoil design [33]. To further hasten the discovery of local optima, the use of a selective line search is also investigated [34].

1.4 Research Objective

This paper will examine the feasibility of the use of SMA actuators in a reconfigurable airfoil to increase a wing's lift-to-drag ratio (c_l/c_d) at a subsonic flight condition. The design of the reconfigurable airfoil utilizing a hybrid simplex-genetic algorithm to designate optimal actuator placement will be investigated, and the development of an experimental proof-of-concept reconfigurable wing model will also be addressed. The primary goal of this research is to deform an initially symmetric airfoil section to provide a higher lift-to-drag ratio at a single subsonic flow condition. A demonstration of airfoil reconfigurability will show the ability of SMA actuators to modify the global shape of an existing airfoil. This technology could also then be used to alter other characteristics of the wing, including thickness and twist. The lift-to-drag ratio was selected as a base for the optimization function because of its relation to wing efficiency in aircraft design. The methods presented by this research will be applicable to any desired design fitness function, including aerodynamic, structural, and energy-based characteristics. Though the current research focuses on a single subsonic flight condition, these methods can be used to form any number of optimal airfoil shapes across multiple flow regimes.

The following section will discuss the structural and aerodynamic modeling of the airfoil and Section 3 will focus on the implementation of the hybrid genetic algorithm to this design optimization problem. Section 4 will discuss the results of the design optimization. Section 5 will discuss the development of a simplified experimental model to verify the results of the computer model, and Section 6 will describe the reconfigurable wing wind tunnel experiments. Conclusions will be presented in Section 7.

2. STRUCTURAL AND AERODYNAMIC MODELING

The focus of this research is to develop a wing that, starting from an arbitrary airfoil shape, can be deformed into a new airfoil shape that is more efficient at a certain set of flow conditions. The initial airfoil shape was a NACA 0012 and the target flow condition was subsonic at three degrees angle of attack. The placement and actuation strain of the SMA wires within the deformed airfoil was optimized such that the new airfoil would have a higher lift-to-drag ratio (c_l/c_d) than the initial airfoil. The internal structure of the wing was a conventional configuration of spar, ribs, and skin. Care was taken to avoid the introduction of bulky mechanisms that would negate the advantages of the SMA actuators.

The use of SMA actuators inherently calls for a coupled thermomechanical analysis environment [35,36,37]. The achieved actuation strain of the SMA depends on the temperature of the wire and the stress applied on the wire. Aerodynamic forces in the form of a pressure distribution over the wing will also play a role in how the wing deforms, and the resulting deformation of the wing will in turn affect the shape of the pressure distribution. Thus, the coupled thermomechanical structural model will be linked with a subsonic aerodynamic model.

All structural analyses were computed using ABAQUS, a commercial finite element method software package, utilizing user material subroutines to define the SMA material following the model outlined in Appendix A [38,39,40].

Initially, a three-dimensional FEM wing model was developed for structural analysis. The elements used to define the wing skin were four-node stress/displacement shell elements. Steel was selected as the skin material, with a thickness of 0.254 mm. The span and the chord of the wing were 30.48 cm each. Cosine spacing was used to refine the mesh at the leading and trailing edges. Fixed boundary conditions in six degrees of freedom (3 rotation, 3 translation) were applied on part of the top and bottom surfaces along the span of the wing to simulate the attachment of the skin to internal load-bearing structures, and 0.5 mm diameter SMA wires were located at four evenly spaced locations along the span, approximately 7.6 cm apart.

It became readily apparent that the three-dimensional model would be too computationally expensive to be efficient as part of a design optimization tool. A two-dimensional FEM model was then developed to simulate the three-dimensional FEM model by assuming an equivalent distribution of SMA actuation along the span of the wing. For optimization purposes, a wire spacing of 20 cm was used. This resulted in an order of magnitude reduction in computation time for the simulation. The airfoil skin was composed of four-node bilinear plane strain elements. The dimensions of the wing (i.e., chord length, skin thickness) remained the same as in the three-dimensional case. The two-dimensional finite element model is shown in Figure 2, and Figure 3 is a detail of the leading edge elements.

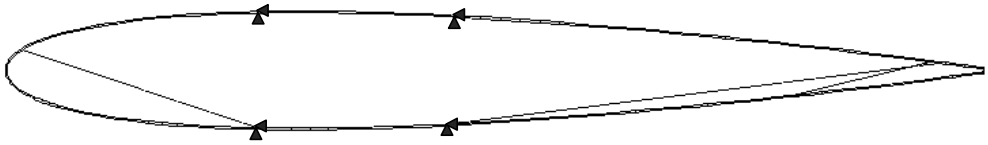

Figure 2. Geometry of reconfigurable wing used for the 2-D FEM analysis with placement of actuators shown

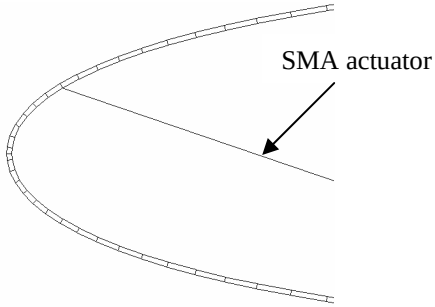

Figure 3. Leading edge elements and SMA wire connection point

The subsonic computational fluid dynamics code utilized in this research was XFOIL, developed by Mark Drela of MIT [41,42]. XFOIL is a modified panel method code used to calculate both viscous and inviscid flow about a 2-dimensional body. The mesh defining the CFD model was exported directly from the FEM output using a Fortran subroutine. For CFD analysis, the design flight conditions were kept fixed at 3 degrees angle of attack and a Reynolds number of 10^7. These values were chosen to keep the design optimization simplified in the early stages of its development, though it is feasible – and indeed, necessary – that multiple flight conditions be included in future optimization routines. Figure 4 details the staggered strategy used for coupling the thermomechanical structural analysis with the aerodynamic analysis. The temperature of the SMA wires is raised from below the austenitic start temperature to well above the austenitic finish

temperature. The temperature increase is divided into approximately 30 increments to reduce the need for multiple iterations at each increment. The first incremental structural deformation is computed by ABAQUS. The resulting deformed shape is captured and used as input to XFOIL. A pressure distribution is computed and returned to ABAQUS to act as an external distributed load on the next increment. The process is repeated until a converged solution is reached within ABAQUS. Convergence is complete when the SMA wires have reached their final temperature and are fully transformed.

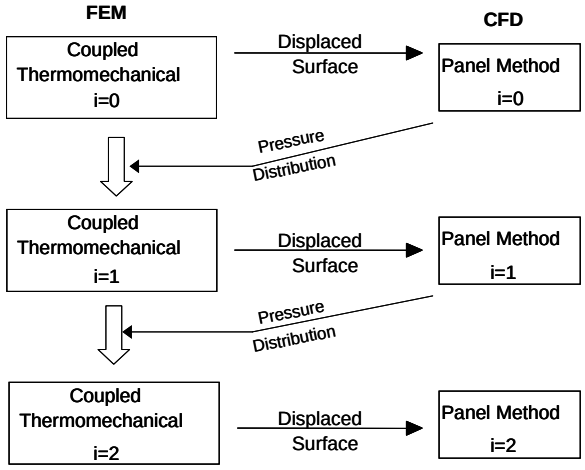

Figure 4. Strategy for coupled aero-thermomechanical analysis

3. GENETIC ALGORITHM AND OPTIMIZATION PROCEDURE

The design problem presented is a complicated one, utilizing several separate analysis codes (structural and fluid dynamics), complex geometry, and non-linear hysteretic material response. A solution consisting of the optimal locations of actuators within the airfoil and their respective transformation strains is desired. A cost function related to aerodynamic performance and subject to structural and aerodynamic constraints was generated, and the genetic algorithm is tasked with finding a minimum cost solution. Because the genetic algorithm is a global search method, it is inefficient alone for such a non-linear optimization problem. A hybrid method incorporating local techniques was combined with the genetic algorithm to decrease the number of fitness evaluations needed to reach an optimal value. The detailed development of the hybrid genetic algorithm optimization procedure can be found in Appendix B.

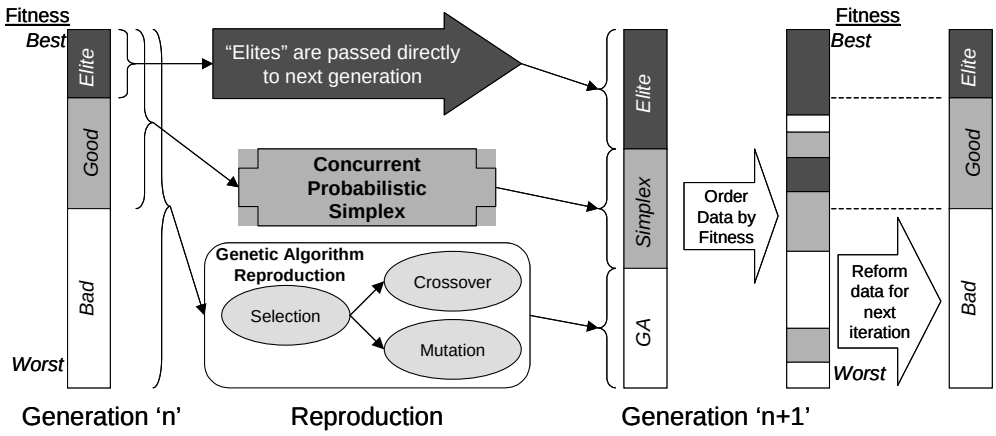

Figure 5. Hybrid simplex-genetic algorithm schematic

Figure 5 shows a schematic of the hybrid simplex-genetic algorithm. When the genetic algorithm evaluates a particular generation, it copies the fittest 10 percent of the chromosomes directly to the next generation. This ensures that the best solutions will remain in the next generation of solutions. After that, the top 40 percent of the chromosomes in the current generation (including the best 10 percent from above) participate in the concurrent probabilistic simplex and line search, and are taken to the next generation. Finally, the entire population of the current generation is subjected to the crossover and mutation operators based on their current fitness.

The hybrid GA-simplex method suits this complex design problem well. Because of the vast solution space and the non-linearity of the problem, the likelihood of other optimization methods (e.g., gradient methods) falling into one of many local minima is very high. Additionally, the GA's intrinsic operating structure of chromosomes and genes closely relates to the design problem's makeup of actuator combinations and their respective properties. In the case of the reconfigurable wing, each chromosome represents a realizable airfoil configuration. Each chromosome is defined by three genes: the first wire endpoint, the second wire endpoint, and the transformation strain. This allows for a straightforward translation from the design problem to the genetic operators of the optimization code. The genetic algorithm software is a modified version of GENESIS [33,43] incorporating a simplex method and line search techniques. All codes were executed on an SGI Origin 2000.

A schematic diagram of the iterative design optimization procedure is shown in Figure 6. The genetic algorithm maintains a set of candidate solutions, and at each iteration, it changes the solution set to one that more accurately satisfies the objectives. However, the quality of the GA's optimal solution is directly related to how accurately the evaluation function captures the design goal. Currently, the evaluation function is based on the lift-to-drag ratio for the airfoil. When the GA needs to evaluate a certain wire configuration, the evaluation function is called.

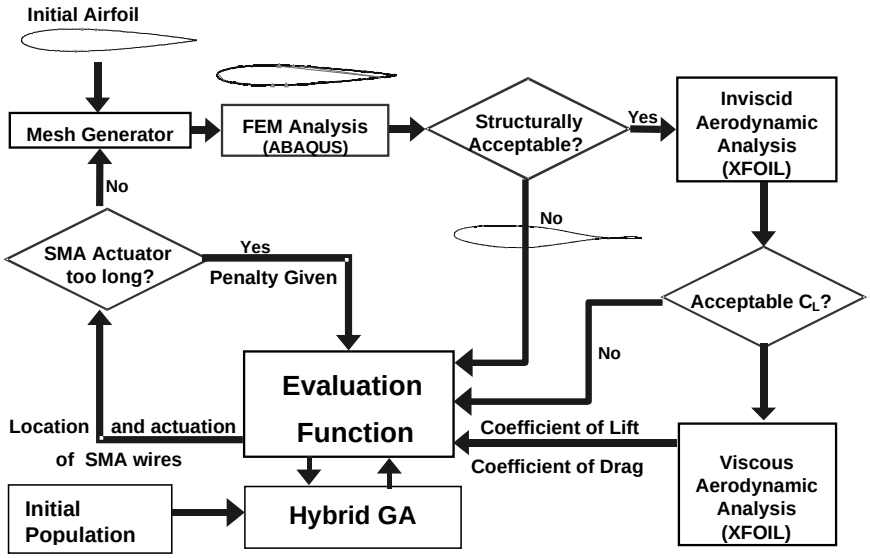

Figure 6. Schematic of the iterative optimization procedure

The first step of the optimization procedure checks to ensure that the SMA actuator is not too long with respect to the chord length of the airfoil. Typically, when the SMA actuator is very long, the likelihood that an acceptable solution will be reached is greatly reduced. Therefore, a penalty is imposed and the structural and aerodynamic analysis steps are skipped.

If the SMA actuator is not too long, then a finite element mesh is generated and used as input to the structural analysis code. The resulting deformed airfoil is then evaluated to determine whether it is structurally feasible. To minimize computational cost, contact forces between the upper and lower airfoil surfaces are not evaluated, making it possible for the two surfaces to pass through one another during the FEM analysis. A simplified surface contact detection code was written to check for such a case. Instead of continuing with the analysis, these physically impossible solutions are given an imposed penalty and the aerodynamic analysis step is skipped.

If the structure is acceptable, it is then passed to the first aerodynamics step for inviscid analysis. The inviscid analysis typically takes much less computation time than a viscous analysis, but values for drag are not calculated. If the coefficient of lift, c_l, is higher than 0.08, the model will continue to be analyzed in a viscous analysis. Otherwise, the viscous analysis step will be skipped and a penalty added to the evaluation function. This value of c_l was chosen to eliminate solutions with negative or very small lift coefficients.

Finally, if the airfoil has an acceptable inviscid lift coefficient, it is analyzed in a viscous CFD analysis. From this, the viscous coefficient of lift and the coefficient of drag are returned to the evaluation function. This entire evaluation procedure is summarized in Table 1.

The genetic algorithm requires three input variables per wire – the location of the top surface point, the location of the bottom surface point, and amount of actuation of the wire. Constraints for these three variables are such that the top surface point can only be chosen from the top surface of the model, and the bottom surface point can likewise only be chosen from the bottom surface of the model. The amount of actuation (or transformation strain) can fall between 0.5% and 5.0%.

Table 1. Summary of Evaluation Function Chain

Optimization Parameters	9 variables: endpoint 1, endpoint 2, and actuation strain for each of 3 SMA wires
Evaluation Function (cost function)	If length of any wire is greater than 50% of the airfoil chord then *SMA too long:* $E_1 = A_1 + B_1$*Wire length Else if distance between upper and lower surface of deformed airfoil is less than 10% of maximum thickness then *Not structurally acceptable:* $E_2 = A_2 + B_2$*Distance between top and bottom surfaces Else if the inviscid coefficient of lift is less than 0.08 then c_l *not acceptable:* $E_3 = A_3 - B_3 * c_l$ Else complete viscous analysis and finish iteration: $E_4 = A_4 - B_4 * c_l / c_d$
Variable Description	c_l, c_d are aerodynamic coefficients of lift and drag A_i, B_i are normalization constants chosen such that: $E_1 > E_2 > E_3 > E_4$

A convergence study was performed on a three-actuator reconfigurable airfoil optimization case to compare the relative convergence rates of the GA alone, the simplex method alone, and the hybrid simplex-GA optimization method. The results in Figure 7 show that hybrid simplex-GA converges faster than either method in stand-alone form. An additional convergence study was conducted to determine the performance of the line search method. The results in Figure 8 show that the line search method brings a quicker convergence than the hybrid simplex-GA alone.

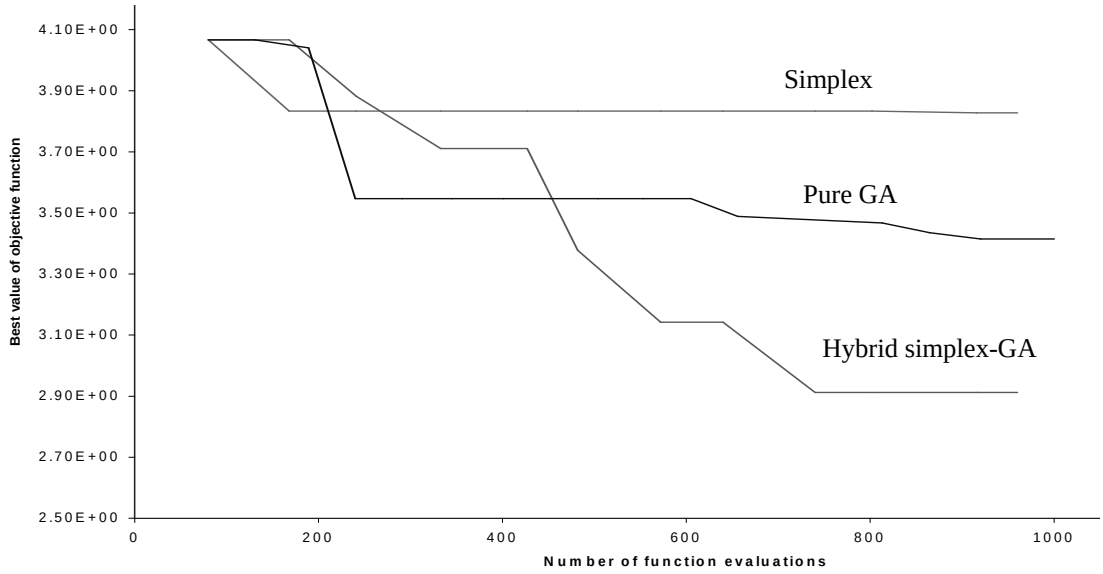

Figure 7. Convergence comparison of GA, simplex, and hybrid simplex-GA methods

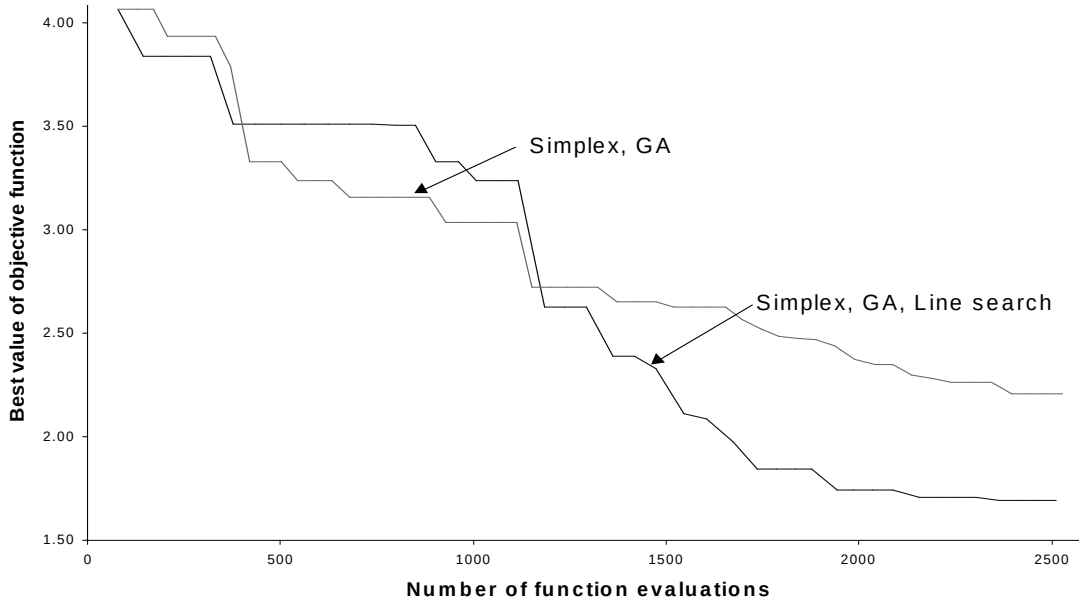

Figure 8. Convergence study of line search method

4. DESIGN OPTIMIZATION RESULTS

The results of the optimization procedure including the aero-thermo-mechanical analysis and evaluation function are presented in this section. A symmetric airfoil, NACA 0012, was selected as the initial airfoil. The goal of this design optimization is to maximize c_l/c_d. Figure 9 shows the pressure distribution results of a viscous analysis of the initial airfoil at the proposed flight conditions: a Reynold's number of 10^7 at three degrees angle of attack. A lift-to-drag ratio of about 50 was returned.

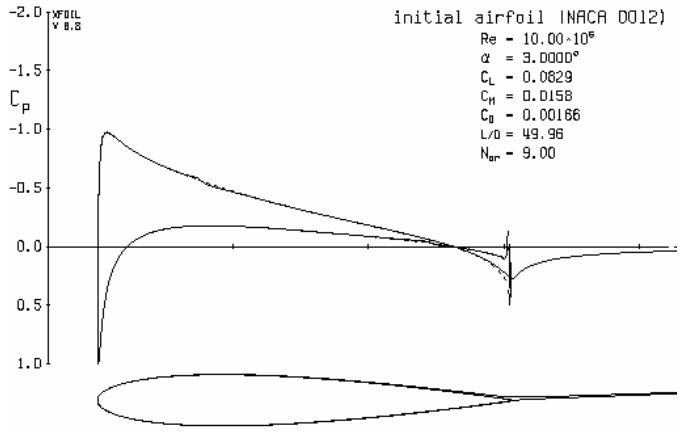

Figure 9. Viscous analysis of NACA 0012 airfoil

The wire configuration solution found by the genetic algorithm for reconfiguring a NACA 0012 airfoil at three degrees angle of attack is shown in Figure 10. There are three SMA wire actuators, whose transformation strains are designated beside their respective arrows, and whose material properties have been outlined in Appendix A. The four triangles near the airfoil's midsection are the zero-displacement boundary conditions imposed during structural analysis. These points were chosen to help bias the optimal solution, thus reducing the number of bad solutions, while maintaining a feasible representation of a wing's internal structure. The resulting deformed shape is shown in Figure 11. Note that both the leading edge and trailing edge are drooped, effectively creating camber across the airfoil.

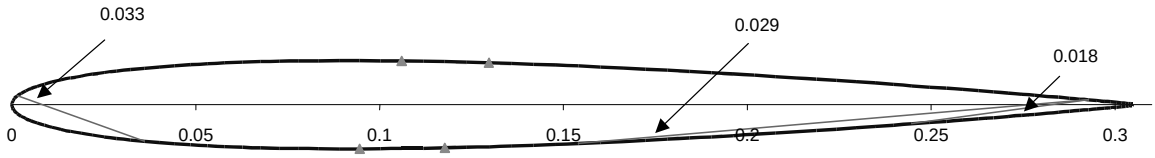

Figure 10. Optimal SMA actuator configuration from genetic algorithm with transformation strain shown for each SMA actuator

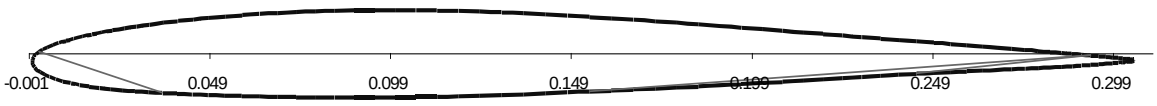

Figure 11. Deformed shape after SMA actuation

The pressure distribution from the viscous analysis of the resulting airfoil is shown in Figure 12. The lift-to-drag ratio of the deformed airfoil is 72.8 – roughly 45 percent higher than that of the original airfoil.

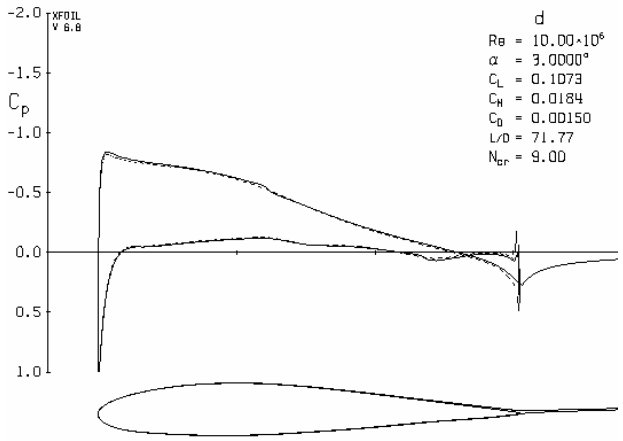

Figure 12. Viscous analysis of GA-optimized deformed airfoil

Viscous analyses of both the original and the resulting airfoils were also performed at two and four degrees angle of attack, and also showed an improvement in c_l/c_d.

5. EXPERIMENTAL MODEL DEVELOPMENT

A fully operational reconfigurable model has been developed primarily as a proof of concept, but also to experimentally verify the structural and aerodynamic results of the design optimization.

5.1 Small-Scale Reconfigurable Wing Model

The model has a chord of 30.48 cm. and a span of 30.48 cm. The initial undeformed airfoil is a NACA 0012. Four SMA wire locations were designated near the leading edge along the span of the wing. Experience with the optimization code has shown that trailing edge deflections have had the most effect on increasing the lift-to-drag ratio. However, workable volume in the trailing edge of the wing at this scale was minimal. It was determined that only leading edge wires could be implemented in this experiment. The leading edge wire locations were determined by the optimization efforts outlined in this paper. To instigate trailing edge deflections using only leading edge wires, load must somehow be transferred across the zero-deflection boundary conditions. Therefore, in the interest of generating a measurable change in the lift-to-drag ratio, the upper surface boundary conditions were removed to facilitate the transfer of load across the top surface of the model[1]. The thickness of the ABS skin provides enough stiffness to resist aerodynamic load deformation at this scale.

The optimization model was based on ideal conditions, but the development of the experimental wing introduced some implementation issues. The connection of SMA wire actuators to the skin ultimately resulted a 300% increase in SMA wire length, due to flex in the linkage system. The available SMA wire had a cross-sectional area half the size of those used in the optimization; therefore two wires were placed at each wire location. A new structural FEM model was developed to verify the design changes. Originally, a steel-skin model was developed and achieved a trailing edge deflection of approximately 3.0 mm., compared to a predicted value of 3.1 mm. It was not fit for wind tunnel testing, and the ABS skin model was developed. The ABS skin model is shown in Figure 13. The figure shows the layout of the internal structural members of the wing.

[1] Though the authors acknowledge that this might seem unrealistic on a manned-flight scale, the reader is reminded that unmanned vehicles are not subject to the same size and weight restrictions, and this type of structure may yet prove feasible. Aircraft design feasibility aside, this is a proof of concept effort on a small scale model. Future work involving experimental wings on a larger scale will be the only way to truly verify the full multi-wire optimization.

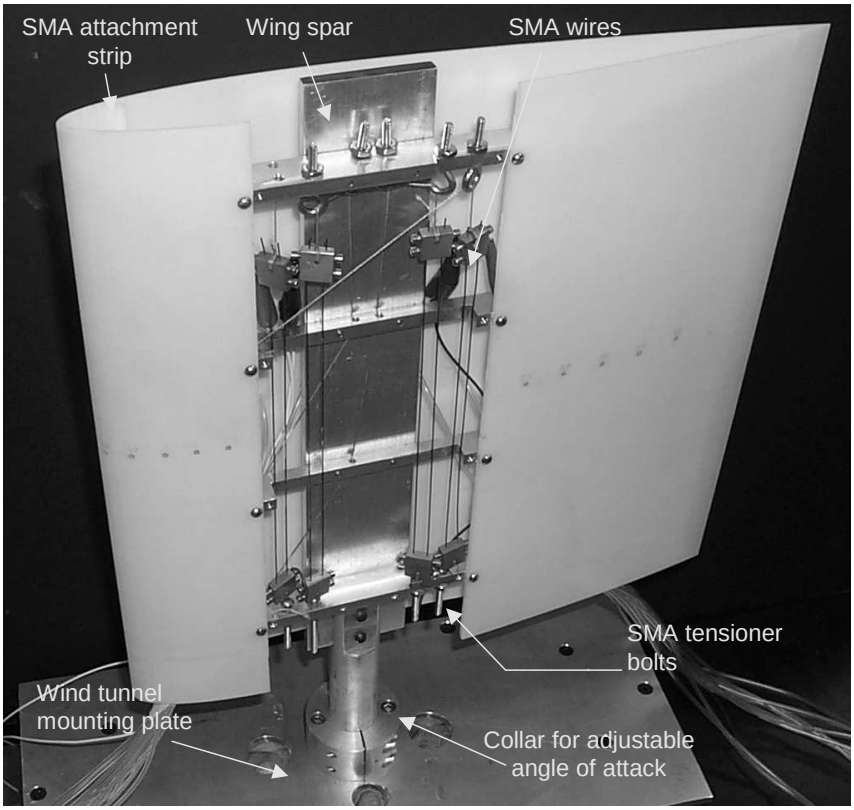

Figure 13. Second-generation prototype wind tunnel model

The FEM analysis (modified to account for the implementation issues discussed above) is shown in Figure 14. A trailing edge deflection of 5.0 mm was predicted. Figure 15 shows a cross-sectional view of the aft wing section in an undeformed state. Figure 16 shows an identical camera angle of the model in a fully actuated position, and shows a trailing edge deflection of approximately 6 mm. The difference between the predicted deflection and the actual deflection arises from the rough experimental measurement technique and the complex factors in design as well as the fact that the numerical solution assumed a uniform and homogeneous skin material, when in actuality this assumption is not strictly correct.

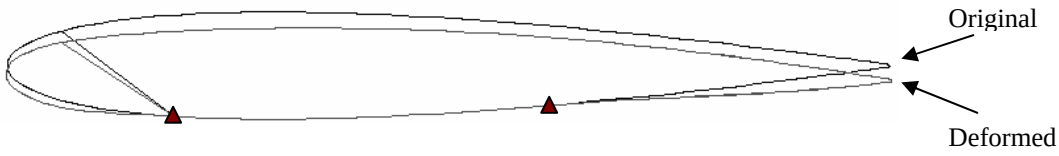

Figure 14. FEM analysis of ABS plastic-skin wing

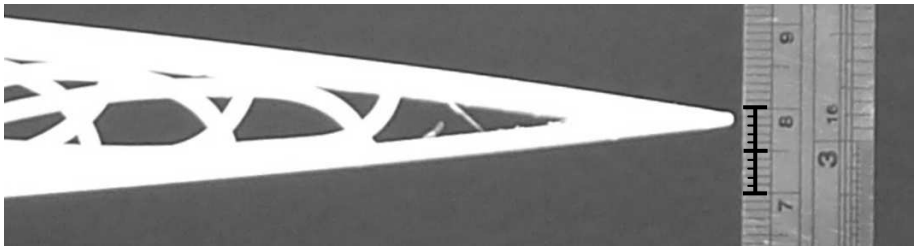

Figure 15. Trailing edge, undeformed state

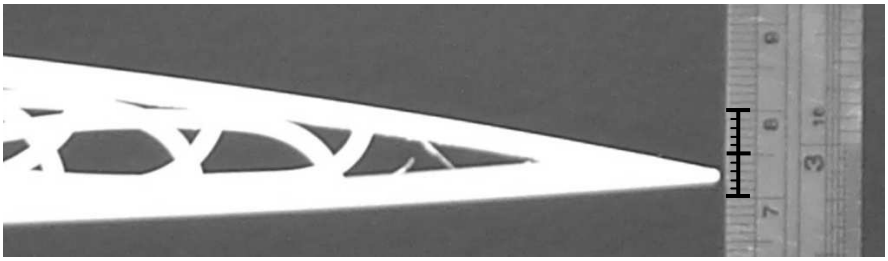

Figure 16. Trailing edge, actuated state

6. WIND TUNNEL TESTING

The goal of these tests was to measure the pressure distribution over the original and deformed airfoil shapes to verify that an increase in lift was being achieved. The pressure data must be reduced into a non-dimensional coefficient of pressure term, C_P. C_P is calculated as follows:

$$C_P = \frac{p - p_\infty}{\frac{1}{2}\rho V^2} = \frac{p - p_\infty}{q} \tag{1}$$

where $p - p_\infty$ is the differential pressure measured by an electronically scanned pressure (ESP) instrument. This differential pressure is normalized with respect to the dynamic pressure, q, which is a function of density, ρ, and free-stream velocity, V. If the flow is incompressible and no Mach effects are observed, the C_P pressure distribution should be the same regardless of flow velocity.

The non-dimensional normal force coefficient can be determined from the pressure distribution data by integrating between the upper and lower pressure distribution curves as follows:

$$c_n = \frac{1}{c}\int_0^c \left(C_{p,lower} - C_{p,upper}\right)dx \tag{2}$$

where c is the chord length of the airfoil. Finally, to calculate the coefficient of lift for a given angle of attack, the angle of attack must be corrected for in the normal force coefficient calculation:

$$c_l = c_n \cos\alpha \tag{3}$$

An ESP was used to capture pressure data from 29 ports along the upper and lower surfaces of the wing. More ports were desired to increase resolution, but the available space within the model limited the number.

Figure 17 shows the actual configuration of the lower surface pressure ports on the wing mounted in the wind tunnel.

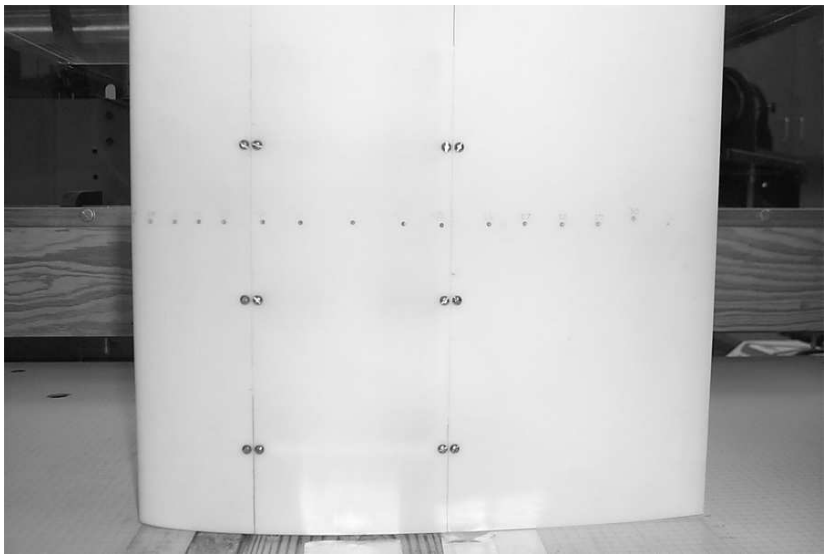

Figure 17. Lower surface of wing showing pressure port locations

The wind tunnel tests were conducted at the Texas A&M 2'x3' low speed wind tunnel in College Station, Texas. The model was subjected to flow velocities of 8.5, 10.2, and 12.0 m/s. The ambient test conditions were a temperature of 18° C, an atmospheric pressure of 101.1 kPa, and an air density of 1.21 kg/m^3. The model was swept through 0, 5, and 10 degrees angle of attack. An additional 16.0 m/s velocity run was preformed at 0 degrees angle of attack to further examine performance at higher velocities. For each test case, data was taken in the undeformed configuration. Then, the wing was actuated and data was taken in the deformed configuration.

6.1 Wind Tunnel Experimental Results

It is first prudent to verify that the flow is incompressible at the test velocities. Figure 18 shows the effect of velocity on pressure distribution over the undeformed wing at five degrees angle of attack and Figure 19 shows the same effect on the deformed wing. As noted earlier, for incompressible flow, the normalized pressure distributions should be identical. There is some small experimental error to be expected, so the velocity sweep data was used to calculate a mean pressure distribution for a given wing state (undeformed or deformed) for a particular angle of attack (0, 5, or 10 degrees). These mean pressure distributions will be used to compare experimental results with numerical results.

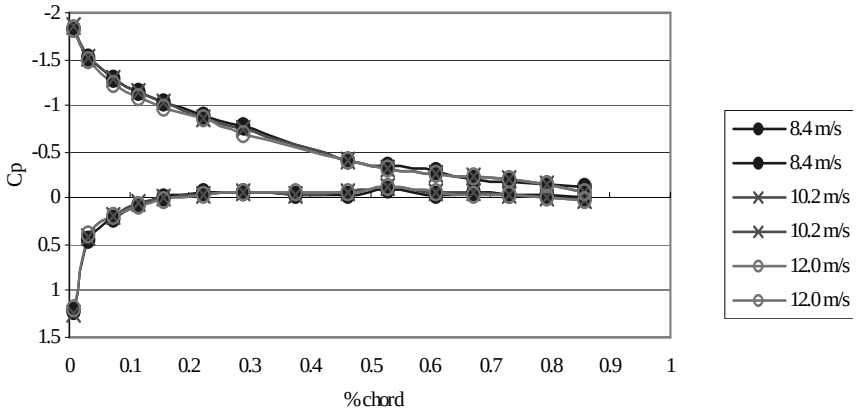

Figure 18. Velocity sweep, undeformed case, 5° angle of attack

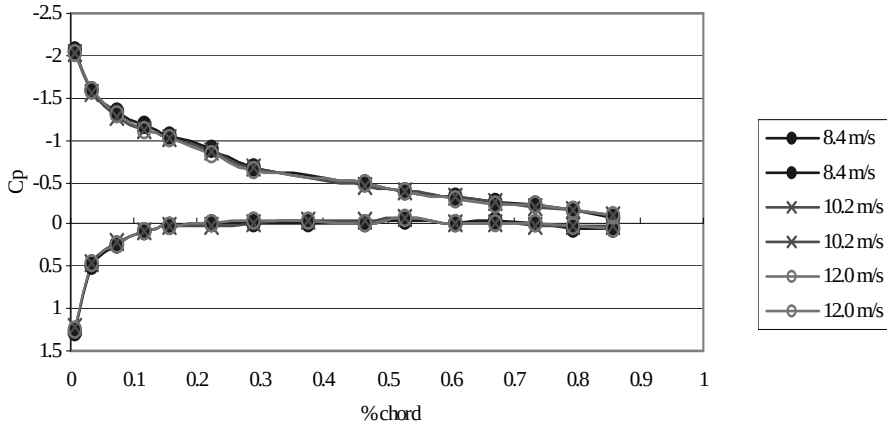

Figure 19. Velocity sweep, deformed case, 5° angle of attack

The next series of figures shows the deformed vs. undeformed case pressure distributions for each angle of attack. Figures 20, 21, and 22 show this comparison at 0, 5, and 10 degrees angle of attack, respectively.

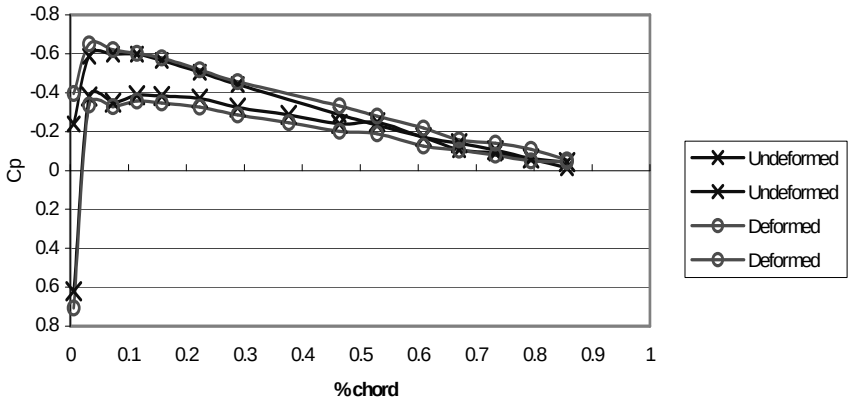

Figure 20. Effects of deformation on pressure distribution, 0° angle of attack

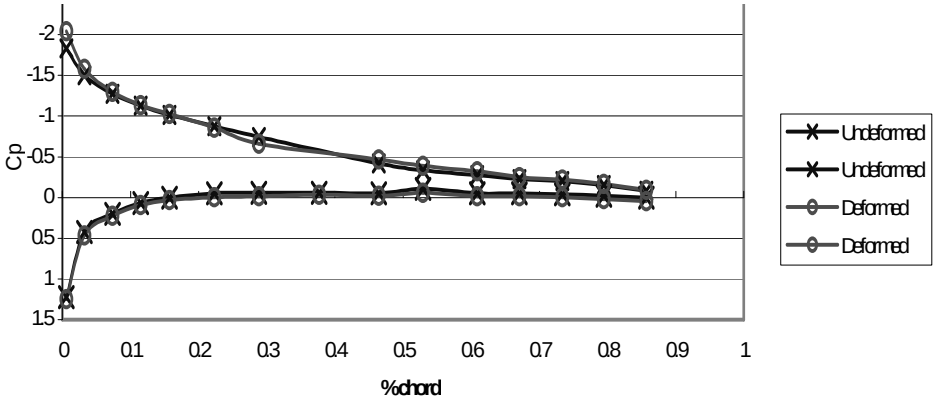

Figure 21. Effects of deformation on pressure distribution, 5° angle of attack

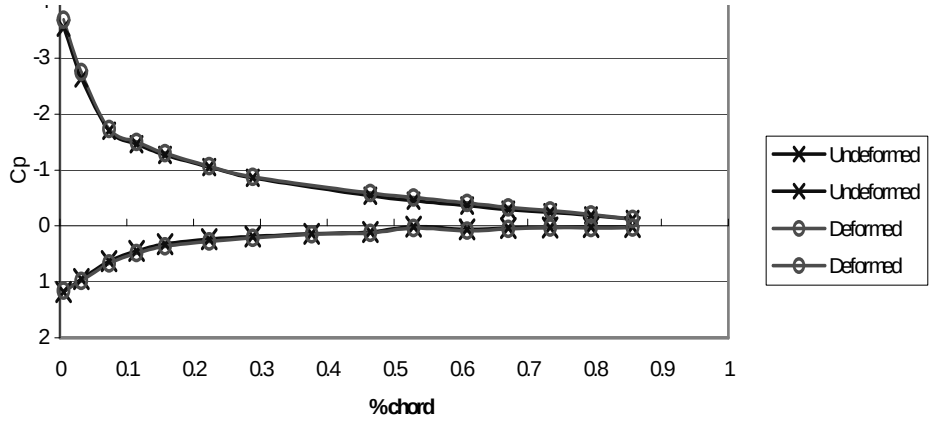

Figure 22. Effects of deformation on pressure distribution, 10° angle of attack

Curves were fit to the data and the integral between the upper and lower surfaces was calculated to find the lift coefficient, c_l. Table 2 shows the results of those calculations.

Table 2. Change in lift coefficient due to SMA actuation

Angle of Attack	Lift Coefficient-Undeformed case	Lift Coefficient-Deformed Case	Δc_l	% increase
0	0.072	0.134	0.062	N/A
5	0.510	0.555	0.045	8.79%
10	0.837	0.892	0.055	6.59%

The greatest improvement in c_l is at zero degrees angle of attack, with an increase of about 0.062. At five and ten degrees angle of attack, increases of 0.045 and 0.055, respectively, were observed.

6.2 Comparison of Experimental and Numerical Results

Computational fluid dynamics calculations were performed on the original and deformed airfoil shapes for 0, 5, and 10 degrees angle of attack. The next six figures show an overlay of these numerical pressure distributions over the average pressure distributions calculated from the velocity sweep shown in Figures 23-28. Figures 23 and 24 show the comparison of experimental vs. numerical pressure data at zero degrees angle of attack for the undeformed and deformed cases. Figures 25 and 26 show similar data for five degrees angle of attack, and Figures 27 and 28 show the pressure comparison data for ten degrees angle of attack.

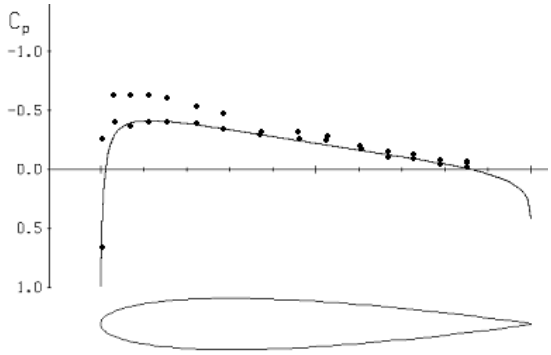

Figure 24. Numerical vs. experimental pressure data, undeformed case, 0° angle of attack

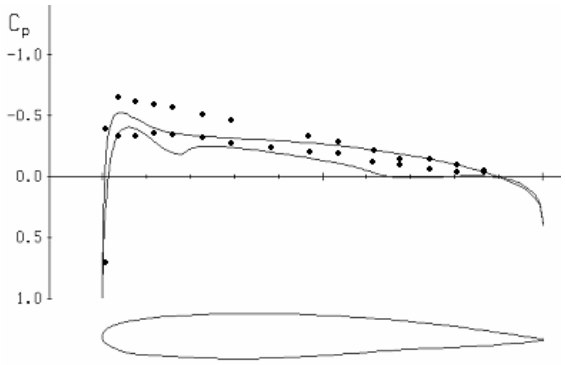

Figure 25. Numerical vs. experimental pressure data, deformed case, 0° angle of attack

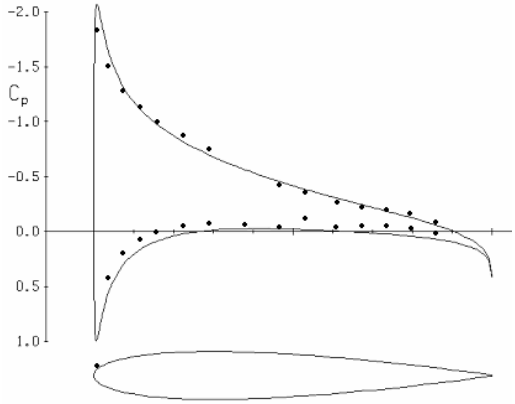

Figure 26. Numerical vs. experimental pressure data, undeformed case, 5° angle of attack

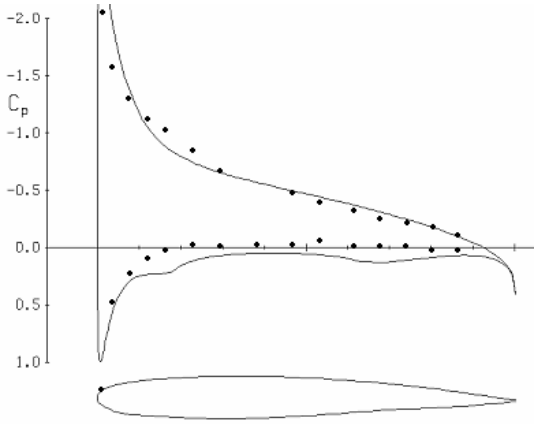

Figure 27. Numerical vs. experimental pressure data, deformed case, 5° angle of attack

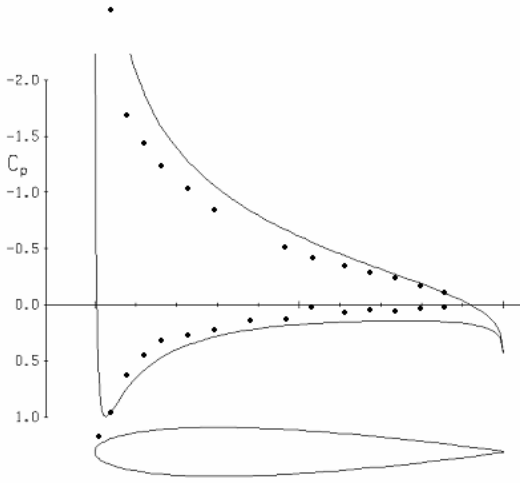

Figure 28. Numerical vs. experimental pressure data, undeformed case, 10° angle of attack

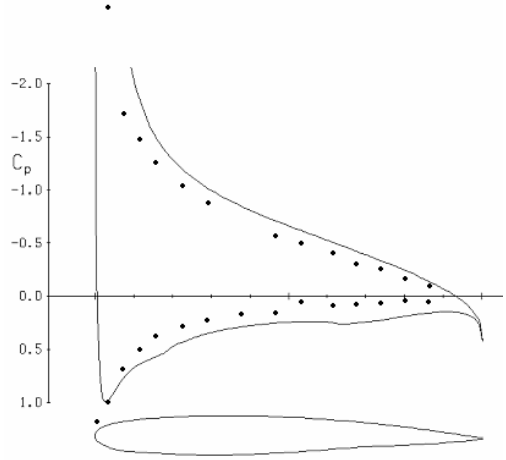

Figure 29. Numerical vs. experimental pressure data, deformed case, 10° angle of attack

At zero degrees angle of attack, the numerical lift is zero, indicating a symmetric undeformed airfoil. The numerical data for the deformed airfoil at zero degrees angle of attack shows some lift, indicating that camber was achieved. The experimental pressure distribution matches the numerical pressure distribution fairly well for the undeformed case. For the deformed case, however, it is necessary to note that while the experimental pressure distribution follows the general trend of the predicted numerical distribution, some details do not appear as expected in the experimental data. A comparison of the Δc_l for the computational and experimental data is shown in Figure 30. The experimental data shows a Δc_l that is approximately half that predicted by the numerical data. While it is not as high as expected, there is a demonstrated increase in lift due to SMA actuation in the reconfigurable wing.

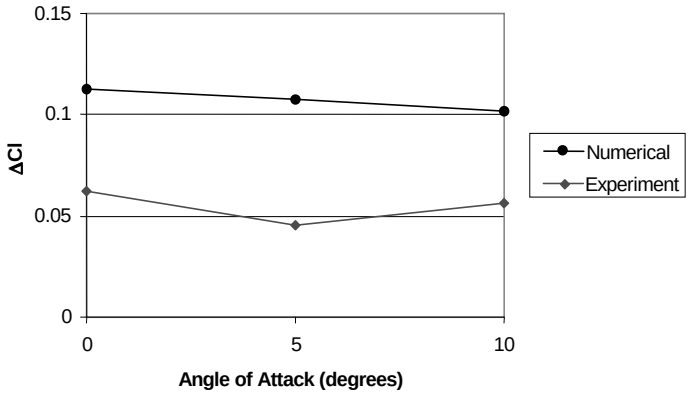

Figure 30. Δc_l vs. angle of attack for experimental and analytical data

7. SUMMARY

The reconfigured airfoil shape is greatly dependant upon the original airfoil shape, the boundary conditions imposed on the airfoil, and the location and transformation strain of the SMA wire actuators. An integrated finite element analysis/computational fluid dynamics environment was developed with the capability of incorporating the thermomechanical response of the SMA actuators to simulate the structural response and aerodynamic characteristics of a reconfigurable wing. This staggered-coupled analysis environment was heavily used as a design tool.

A hybrid simplex-genetic algorithm has been introduced as the primary design optimization method. This method combined a stochastic global search method with several local search methods to achieve an optimal solution. The optimal solution in this case was for three SMA wires embedded in a symmetric NACA 0012 airfoil section. The goal of the design optimization was to achieve a reconfigured airfoil shape that had the highest lift-to-drag ratio at a 3° angle of attack in subsonic flow conditions. A 45% increase in the lift-to-drag ratio was predicted for the optimal case found by the GA.

A reconfigurable wing model was then developed to verify the structural and aerodynamic response predicted by the computational analyses. The ABS skin prototype reconfigurable wing model was developed after unforeseen manufacturing difficulties were overcome. A rapid prototyping machine was used to create an ABS plastic skin with the accurate initial airfoil shape. Actuator attachment points were designed into the skin.

Structural and aerodynamic analyses were performed on the reconfigurable wing model. The structural analysis predicted a trailing edge deflection of approximately 5.0 mm. For comparison purposes, the

experimental trailing edge deflection measured in the bench test was about 6.0 mm. Wind tunnel tests were conducted to obtain experimental pressure distribution data over the original wing shape and the deformed wing shape. These experimental pressure distributions compared well to the numerical pressure distributions for the undeformed case. For the deformed case, the experimental data matched less closely, but still followed the expected trends.

The lift coefficient increased by 0.062 at zero degrees angle of attack when the wing was deformed, by 0.045 at five degrees angle of attack, and by 0.055 at ten degrees angle of attack. This is comparable to the lift increases seen by other researchers. Scherer, et al [24], for instance, achieved a Δc_l that ranged from 0.03 to 0.09, based on SMA-actuated trailing edge flap deflections. The Δc_l that was achieved by the SMA reconfigurable wing is still somewhat lower than the value predicted by the numerical simulations. Despite this, an increase in c_l was observed at all angles of attack, indicating the successful operation of the SMA reconfigurable wing in wind tunnel conditions.

The design methods presented in this paper combined a coupled thermomechanical structural analysis with a subsonic aerodynamic analysis. These analyses were then used to form a fitness evaluation function that could be used by a hybrid genetic algorithm to find the optimal SMA wire actuator placement within a wing to achieve the highest efficiency at a certain set of flow conditions with a given initial wing shape. This research has begun to show the possibilities presented by the SMA actuated reconfigurable wing concept and has presented a foundation for design optimization to implement this technology.

8. ACKNOWLEDGEMENTS

The authors acknowledge the financial support of the U.S. Air Force Office of Scientific Research (grant no. F4 9620-01-1-0196). The authors would also like to acknowledge Dr. Othon Rediniotis and Dr. John Valasek for their assistance in this project.

9. REFERENCES

1. Anderson J D 1978 *Introduction to Flight* (New York: McGraw-Hill)
2. Rediniotis O K, Ko J, Yue X and Kurdila AJ 1999 Synthetic Jets, Their Reduced Order Modeling and Applications to Flow Control *AIAA 99-1000*
3. Englar R J 2000 Circulation Control Pneumatic Aerodynamics: Blown Force and Moment Augmentation and Modification; Past, Present, and Future *Fluids 2000, AIAA 2000-2541* (Denver, CO)
4. Modi V J 2000 On the Moving Surface Boundary-Layer Control *Fluids 2000, AIAA 2000-2238* (Denver, CO)
5. Jacob J D 1998 On the Fluid Dynamics of Adaptive Airfoils Proc. 1998 ASME International Mechanical Engineering Congress and Exposition (Anaheim, CA)
6. Garner L J, Wilson L N, Lagoudas D C and Rediniotis O K 2000 Development of a Shape Memory Alloy Actuated Biomimetic Vehicle *Smart Materials and Structures* **9** 673-683
7. Spillman J J 1992 The Use of Variable Camber to Reduce Drag, Weight, and Costs of Transport Aircraft *Aeronautical Journal* **96** 1-9
8. Austin F, Rossi M J, Van Nostrand W, Knowles G and Jameson A 1994 Static Shape Control for Adaptive Wings *AIAA Journal* **32** 1895-1901
9. Agrawal B N and Treanor K E 1999 Shape Control of a Beam using Piezoelectric Actuators *Smart Materials and Structures* **8** 729-739
10. Chattopadhyay A, Seeley C E and Jha R 1999 Aeroelastic Tailoring using Piezoelectric Actuation and Hybrid Optimization *Smart Materials and Structures* **8** 83-91
11. Lee T and Chopra I 2001Design of a Bidirectional Piezoelectric Actuator for Blade Trailing Edge Flap *Smart Structures and Materials 2001: Smart Structures and Integrated Systems*
12. Pern N J and Jacob J D 1999 Aerodynamic Flow Control using Shape Adaptive Surfaces *Proc. 1999 ASME Design Engineering Technical Conferences* (Las Vegas, NV)

13. Munday D and Jacob J 2001 Active Control of Separation on a Wing with Conformal Camber *39th AIAA Aerospace Sciences Meeting and Exhibit, AIAA 2001-0293* (Reno, NV)
14. Pelinescu I and Balachandran B 2000 Analytical and Experimental Investigations into Active Control of Wave Transmission Through Gearbox Struts *Proc. SPIE* **3985** 76-85
15. Kudva J, Jardin P, Martin C and Appa K 1996 Overview of the ARPA/WL 'Smart Structures and Materials Development – Smart Wing' Contract *3rd SPIE Symposium on Smart Structures and Materials* (San Diego CA)
16. Gilbert W W 1981 Mission Adaptive Wing System for Tactical Aircraft *Journal of Aircraft* **18** 597-602
17. Jardine P A, Bartley-Cho J and Flanagan J 1999 Improved Design and Performance of the SMA Torque Tube for the DARPA Smart Wing Program *SPIE Conference on Industrial and Commercial Applications of Smart Structures Technologies* **3674**
18. Prahlad H and Chopra I 2001 Design of a Variable Twist Tiltrotor Blade Using Shape Memory Alloy (SMA) Actuators *Smart Structures and Materials 2001: Smart Structures and Integrated Systems*
19. Bein T, Hanselka H and Breitbach E 2000 An Adaptive Spoiler to Control the Transonic Shock *Smart Materials and Structures* **9** 141-148
20. Epps J J and Chopra I 2001 In-Flight Tracking of Helicopter Rotor Blades using Shape Memory Alloy Actuators *Smart Materials and Structures* **10** 104-111
21. Kudva J N, Martin C A, Scherer L B, Jardine A P, McGowan A R, Lake R C, Sendeckyj G and Sanders B 1999 Overview of the DARPA/AFRL/NASA Smart Wing Program *SPIE Conference on Industrial and Commercial Applications of Smart Structures Technologies* **3674**
22. Martin C A, Bartley-Cho J, Flanagan J and Carpenter B F 1999 Design and Fabrication of Smart Wing Wind Tunnel Model and SMA Control Surfaces *SPIE Conference on Industrial and Commercial Applications of Smart Structures Technologies* **3674**
23. Scherer L B, Martin C A, West M, Florance J P, Wieseman C D, Burner A W and Fleming G A 1999 DARPA/AFRL/NASA Smart Wing Second Wind Tunnel Test Results *SPIE Conference on Industrial and Commercial Applications of Smart Structures Technologies* **3674**
24. Flemings G A and Burner A W 1999 Deformation Measurements of Smart Aerodynamic Surfaces *44th Annual SPIE International Symposium on Optical Science, Engineering, and Instrumentation* (Denver, CO)
25. Beauchamp C, Nadolink R and Dean L 1992 Shape Memory Alloy Articulated (SMAART) Control Surfaces *ADPA/AIAA/ASME/SPIE Conference on Active Materials and Adaptive Structures*
26. Jackson C M, Wagner H J and Wasilewski R J 1972 55-Nitinol – The Alloy with A Memory: Its Physical Metallurgy, Properties, and Applications *NASA* (Washington D.C.)
27. De Blonk B J and Lagoudas D C 1998 Actuation of Elastomeric Rods with Embedded Shape Memory Alloy Wire Actuators *Smart Materials and Structures* **7** 771-783
28. De Falco L, Del Balio R, Della Cioppa A and Tarantino E 1996 Breeder genetic algorithms for airfoil design optimization *Proc. of IEEE International Conference on Evolutionary Computation* pp. 71-75
29. Jones B R, Crossley W A, Lyrintzis and Anastasios S 1998 Aerodynamic and Aeroacoustic Optimization of Airfoils via a Parallel Genetic Algorithm *AIAA Paper 98-4811, 7th AIAA/USAF/NASA/ISSMO Symposium on Multidisciplinary Analysis and Optimization* (St. Louis, MO)
30. Sadri A M, Wright J R and Wynne R J 1999 Modelling and Optimal Placement of Piezoelectric actuators in isotropic Plates using Genetic Algorithms *Smart Materials and Structures* **8** 490-498
31. Gao F, Shen Y and Luxian L 2000 The Optimal Design of Piezoelectric Actuators for Plate Vibroacoustic Control using Genetic Algorithms with Immune Diversity *Smart Materials and Structures* **9** 485-491
32. Han J and Lee I 1999 Optimal Placement of Piezoelectric Sensors and Actuators for Vibration Control of a Composite Plate using Genetic Algorithms *Smart Materials and Structures* **8** 257-267
33. Yen J, Liao J C, Lee B and Randolph D 1998 A Hybrid Approach to Modeling Metabolic Systems Using a Genetic Algorithm and Simplex Method *IEEE Transactions on Systems, Man, and Cybernetics – Part B: Cybernetics* **28** 173-191
34. Khan M A 2000 Selective Use of Line Search to Improve Hybrid Genetic Algorithm-Simplex Method and its Application to Smart Wing Design Optimization *M.S. Thesis, Texas A&M University*

35. Bo Z and Lagoudas D C 1999 Thermomechanical modeling of polycrystalline SMAs under cyclic loading, Part I: Theoretical derivations *International Journal of Engineering Science* **37** 1089-1140
36. Tanaka K 1986 A Thermodynamical Sketch of Shape Memory Effect: One-Dimensional Tensile Behavior *Res. Mechanica* **18** 251-263
37. Liang C and Rogers C A 1990 One-Dimensional Thermomechanical Constitutive Relations for Shape Memory Materials *Journal of Intelligent Material Systems and Structures* **1** 207-234
38. Lagoudas D C, Bo Z and Qidwai M A 1996 A unified thermodynamic constitutive model for SMA and finite element analysis of active metal matrix composites *Composite Materials and Structures* **3** 153-179
39. Lagoudas D C and Bo Z 1999 Thermomechanical modeling of polycrystalline SMAs under cyclic loading, part II: Material characterization and experimental results for a specific transformation cycle *International Journal of Engineering Science* **37** 1141-1173
40. Bo Z, Lagoudas D C and Miller D A 1999 Material characterization of SMA actuators under non-proportional thermomechanical loading *Journal of Engineering Materials and Technology* **121** 75-85
41. Drela M 1996 Xfoil 6.8 User Primer *MIT Aero &.Astro*
42. Drela M and Giles M B 1987 Viscous-Inviscid Analysis of Transonic and Low Reynolds Number Airfoils *AIAA Journal* **25** 1347-1355
43. Grefenstette J 1984 GENESIS: A system for using genetic search procedures *Proc. 1984 Conf. Intelligent Systems Machines* 161-165
44. Janikow C Z and Michalewicz Z 1991 An Experimental Comparison of Binary and Floating Point Representations in Genetic Algorithms *4th International Conference on Genetic Algorithms* (UC San Diego)
45. Spendley W, Hext G R and Himsworth F R 1962 Sequential Application of Simplex Design in Optimization and Evolutionary Operation *Technometrics* **4** 441-461

APPENDIX A : SMA MODEL

The model defined by these subroutines is a phenomenological constitutive model using a general thermodynamic framework with internal state variables [38,39,40]. A summary of the constitutive SMA model in one-dimensional form is as follows. The Gibb's free energy for the 1-D case can be defined as

$$G = -\frac{1}{2}\frac{1}{\rho}S\sigma^2 - \frac{1}{\rho}\sigma\left[\alpha(T-T_0)+\varepsilon^t\right] + c\left[(T-T_0) - T\ln\left(T/T_0\right)\right] - s_0 T + u_0 + f(\xi) \tag{4}$$

where ρ is the density, S is the compliance, σ is the applied stress, α is the thermal expansion coefficient, ε^t is the transformation strain, c is the specific heat, s_0 is the entropy, u_0 is the internal energy, ξ is the martensitic volume fraction, and $f(\xi)$ is the strain hardening function. S, α, c, s_0, and u_0 are defined in terms of the martensitic volume fraction by a rule of mixtures as

$$\begin{gathered} S = \frac{1}{E^A} + \xi\left(\frac{1}{E^M} - \frac{1}{E^A}\right), \quad \alpha = \alpha^A + \xi\left(\alpha^M - \alpha^A\right) \\ c = c^A + \xi\left(c^M - c^A\right), \quad s_0 = s_0^A + \xi\left(s_0^M - s_0^A\right), \quad u_0 = u_0^A + \xi\left(u_0^M - u_0^A\right) \end{gathered} \tag{5}$$

The strain hardening function is defined as

$$f(\xi) = \begin{cases} \frac{1}{2}\rho b^M \xi^2 + (\mu_1 + \mu_2), & \dot{\xi} > 0 \\ \frac{1}{2}\rho b^A \xi^2 + (\mu_1 - \mu_2), & \dot{\xi} < 0 \end{cases} \tag{6}$$

where ρb^M, ρb^M, μ_1, and μ_2 are transformation strain hardening constants defined as follows:

$$\rho b^A = -\rho\Delta s_0\left(A^{0f} - A^{0s}\right), \qquad \rho b^M = -\rho\Delta s_0\left(M^{0s} - M^{0f}\right) \tag{7}$$

$$\mu_1 = \gamma^p - \rho\Delta u_0, \qquad \mu_2 = \tfrac{1}{4}\left(\rho b^A - \rho b^M\right) \tag{8}$$

$$\gamma^p = \tfrac{1}{2}\rho\Delta s_0\left(M^{0s} + A^{0f}\right) \tag{9}$$

The relationship between transformation strain and the martensitic volume fraction is expressed by

$$\dot{\varepsilon}^t = \Lambda\,\dot{\xi} \tag{8}$$

where Λ defines the transformation strain direction, and is assumed to have the following form:

$$\Lambda = \begin{cases} H\dfrac{\sigma}{|\sigma|} & \dot{\xi} > 0 \\ \dfrac{\varepsilon_r^t}{\xi_r} & \dot{\xi} < 0 \end{cases} \tag{9}$$

where ε_r^t and ξ_r are the transformation strain and martensitic volume fraction at the reversal point of the forward phase transformation, and H is the maximum uniaxial transformation strain for a particular transformation cycle and applied stress. The thermodynamic force conjugate to ξ is defined as

$$\pi = \sigma\Lambda - \rho\frac{\partial G}{\partial \xi}. \tag{10}$$

Substituting equation (4) into equation (9) yields

$$\pi = \sigma\Lambda + \frac{1}{2}\Delta S\sigma^2 + \rho\Delta s_0 - \rho\frac{\partial f}{\partial \xi} - \rho\Delta u_0 + \Delta\alpha\sigma\left(T - T_0\right) - \rho\Delta c\left[\left(T - T_0\right) - T\ln\left(T/T_0\right)\right] \tag{11}$$

where

$$\Delta S = S^M - S^A, \quad \Delta s_0 = s_0^M - s_0^A, \quad \Delta u_0 = u_0^M - u_0^A, \quad \Delta c = c^M - c^A, \quad \Delta\alpha = \alpha^M - \alpha^A \tag{12}$$

and

$$\rho\Delta u_0 = \rho\Delta s_0 T^{eq} \tag{13}$$

where

$$T^{eq} = \tfrac{1}{2}\left(M^{0s} + A^{0f}\right) \tag{14}$$

The transformation function, Φ, is defined in terms of the thermodynamic force in the following manner

$$\Phi = \begin{cases} \pi - Y^*, & \dot{\xi} > 0 \\ -\pi - Y^*, & \dot{\xi} < 0 \end{cases} \tag{15}$$

where Y^* denotes the measure of internal dissipation due to transformation. The evolution of the martensitic volume fraction is constrained by the Kuhn-Tucker conditions,

$$\begin{aligned} &\dot{\xi} \geq 0 \qquad \Phi(\sigma, T, \xi) \leq 0 \qquad \Phi\dot{\xi} = 0 \\ &\dot{\xi} \leq 0 \qquad \Phi(\sigma, T, \xi) \leq 0 \qquad \Phi\dot{\xi} = 0 \end{aligned} \tag{16}$$

Satisfying the 2nd law of thermodynamics leads to the following constitutive equation

$$\varepsilon = -\rho\frac{\partial G}{\partial \sigma} = S\sigma + \alpha\left(T - T_0\right) + \varepsilon^t. \tag{17}$$

The stress is expressed from equation (17) as

$$\sigma = \frac{1}{S(\xi)}\left[\varepsilon - \alpha(\xi)\Delta T - \varepsilon^t\right] \tag{18}$$

This material model only accounts for one-way shape memory effect (SME), while the actual SMA wires used in the reconfigurable wing exhibit two-way SME. However, for modeling and optimization purposes, one-way SME is sufficient to achieve a deformed airfoil shape since the modeling of the return to the original airfoil shape is beyond the scope of the current work.

Experimentally, however, the wires must exhibit two-way SME to achieve the desired actuator effect. There are several ways to achieve two-way SME in shape memory alloy wires, as described by deBlonk et al [27]. Two-way training is achieved by first deforming the specimen under appropriate load in the martensitic phase. Then, the specimen is heated to its austenitic phase and cooled back to a martensitic phase. After many cycles, the specimen will begin to exhibit two-way shape memory effect. The K type NiTiCu SMA wires used in this work were 152 mm in length and had a diameter of 0.59 mm. The wires were trained by loading them to 372 MPa and cycling fifty 0ºC to 100ºC thermal cycles. A temperature-displacement curve showing four training cycles is shown in Figure 35.

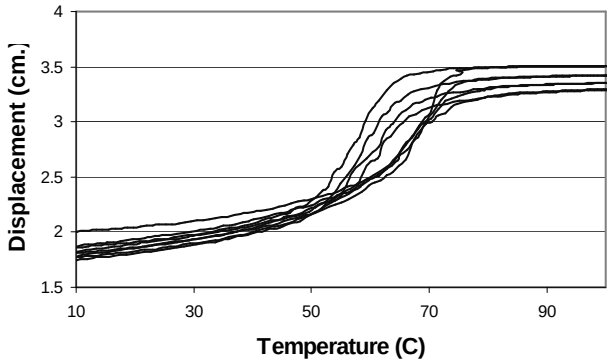

Figure 35. Four SMA wire training cycles

In this work, the wires are heated by electrical current and cooled by natural convection. The wires were put through a series of tests and demonstrated recoverable transformation strain of about 3.7%. A differential scanning calorimeter was used to determine the start and finish austenite and martensite transformation temperatures. The resulting DSC curve is shown in Figure 36. Quasi-static force-displacement tests were conducted on a load frame to determine the modulus of elasticity for both the martensitic and austenitic phases of the material. A summary of the material properties used to model SMA in this research is shown in Table 3.

Table 3. SMA wire material properties

A^{0s}	53.7 °C
A^{0f}	59.5 °C
M^{0s}	45.7 °C
M^{0f}	39.3 °C
E_A	65 GPa
E_M	20 GPa
H	0.136
ν	0.33
α^M	10.0E-6 / °C
α^A	10.0E-6 / °C
$\rho\Delta s_0$	-9.52E6 MPa / °C

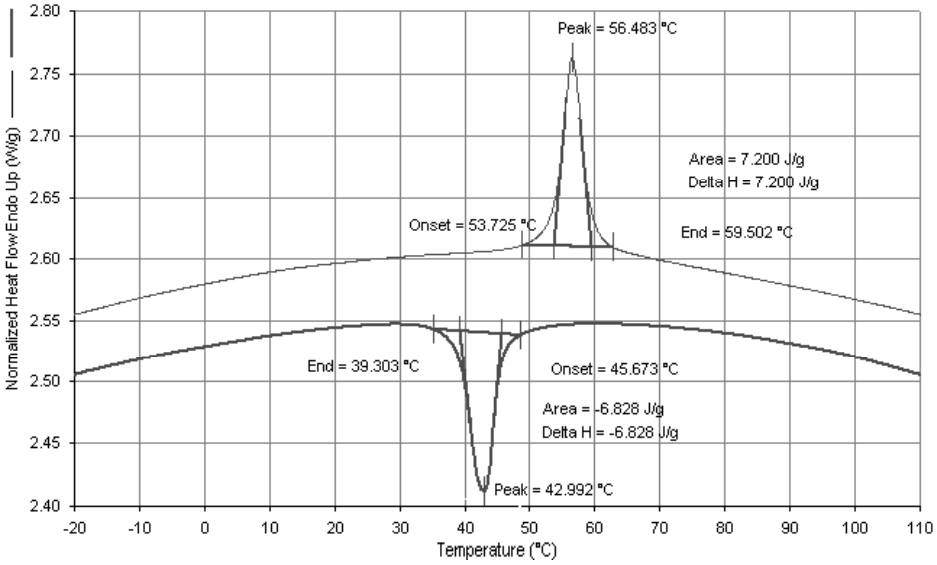

Figure 36. DSC curve of SMA wires

APPENDIX B – GENETIC ALGORITHM

The genetic algorithm requires the evaluation of a fitness function at a number of solutions. Each solution is typically coded in a binary string called a chromosome, and a set of these chromosomes forms a population. This population will "evolve" over the course of several generations until a satisfactory solution is reached. To make GAs better suited for numerical optimization problems, real-coded GAs can be utilized in the place of their binary-coded counterparts. In the real-coded GA, each variable (gene) of the problem domain is represented by a floating point number in the chromosome. The real-coded GA has been shown to outperform the binary-coded GA in continuous problems, and will be utilized in this research [28,44].

The evolution from one generation to the next involves three steps. First, the current population is ranked using a fitness evaluation function. Second, the GA stochastically selects parents from the current generation with a bias towards fitter chromosomes. Third, the GA reproduces offspring from the selected parents using the genetic operators of crossover and mutation. The crossover operator exchanges information between two chromosomes, and the mutation operator alters randomly chosen bits of a chromosome. The crossover and mutation probabilities dictate how often these genetic operators are applied to a population. A non-uniform mutation operator is recommended for the real coded GA. In this mutation, a random integer, p, between zero and one is chosen, and the gene x_k is mutated as follows:

$$x_k = \begin{cases} x_k + (x_{\max} - x_k)\left(1 - r^{\left[1-\left(\frac{t}{T}\right)\right]^b}\right) & \text{p = 0} \\ x_k + (x_{\min} - x_k)\left(1 - r^{\left[1-\left(\frac{t}{T}\right)\right]^b}\right) & \text{p = 1} \end{cases} \tag{19}$$

Where x_{max} and x_{min} are the upper and lower bounds of x_k, respectively, r is a random real number between 0 and 1, T is the total number of generations, t is the current generation, and b defines the rate at which the range of mutation is narrowed over the course of the GA's iterations [34].

This hybrid simplex-GA method considers a minimization of a function of n variables by choosing n+1 points in n-dimensional space. These points, denoted as X_0, X_1, … , $X_{(n+1)}$, define the current "simplex" [45]. The method then forms new simplices by reflecting the worst point X_w with respect to the centroid of rest of the points. The worst point is then replaced by the reflected point, denoted by X_r, such that

$$X_r = \overline{X} + \delta\left(\overline{X} - X_w\right) \tag{20}$$

where the reflection coefficient, δ, is unity for the simplest case, and

$$\overline{X} = \frac{1}{N}\left(X_1 + X_2 + \cdots + X_{w-1} + X_{w+1} + X_{N+1}\right) \tag{21}$$

Figure 37 shows an example of a three dimensional simplex [33]. In Figure 37(a), A and B are good points, D and E are the worst points, C is the centroid of A and B, and D' and E' are the points resulting from the reflection of D and E across C, respectively.

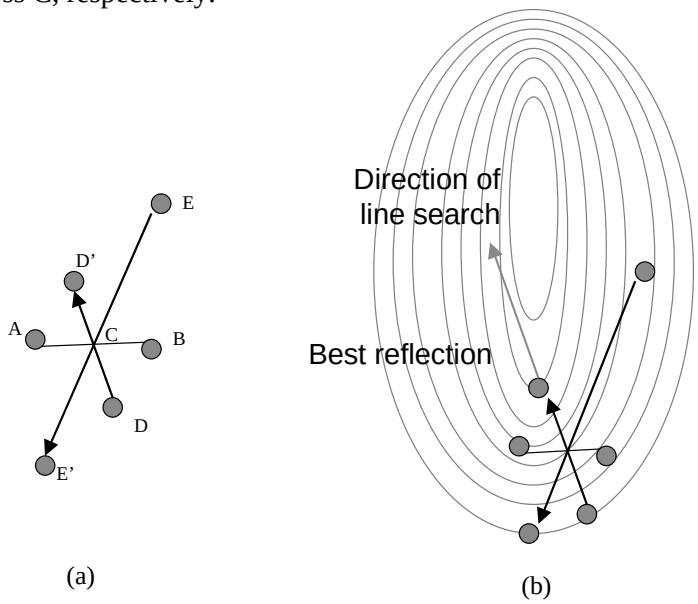

Figure 37. Simplex diagram for a two-dimensional optimization problem

Nealder and Mead proposed a modification of the simplex algorithm by introducing expansion and contraction operators. If the reflected point is better than the current minimum, a better minimum is sought by choosing a point further along the reflection dimension. This is referred to as expansion. On the other hand if the new point becomes the worst or second worst point, it is replaced by a point lying between the centroid and the current worst point. This operation is called contraction. If the result of the contraction is still the worst, then every point X_i is replaced by $(X_I+X_b)/2$ where X_b is the best point. Better convergence rates with the hybrid GA are achieved by starting with $n+k$ points instead of $n+1$ and reflecting k worst points simultaneously, while also using random expansion/contraction coefficients instead of fixed ones. This strategy is called concurrent probabilistic simplex [33]. Additionally, if this simplex operator generates a new best point, then a more precise line search is applied to continue searching for local optima in this promising direction, as shown in Figure 37(b) [34].

Parameters used in the genetic algorithm are shown in Table 4. These parameters are chosen based on experience gained while running the code. If the population size is too small the GA converges early to a sub-optimal value. On the other hand, a large population size may fail to converge within an acceptable number of

iterations. The percentage of chromosomes acted on by the simplex operator determines how much emphasis is given to local exploration by the GA. The optimization code was executed for a number of different population sizes, mutation rates, and simplex percentages and the values shown returned the most optimal value after 1000 evaluations. The number of evaluations was limited because of the time it takes to perform structural analysis and aerodynamic calculations for the evaluation of each chromosome.

Table 4. Parameters used in Genetic Algorithm

Number of genes per chromosome	9
Size of population per generation	80
Percentage of chromosomes to simplex	40%
Crossover probability	0.6
Mutation probability	0.02